Hole doping double perovskites $Sr_2FeMo_{1-x}O_6$ (x = 0, 0.03, 0.04, 0.06) and their Mössbauer, crystal structure and magnetic properties

2008 J. Phys.: Condens. Matter 20 175213

(http://iopscience.iop.org/0953-8984/20/17/175213)

J. Phys.: Condens. Matter **20** (2008) 175213 (9pp) doi:10.1088/0953-8984/20/17/175213

Hole doping double perovskites $Sr_2FeMo_{1-x}O_6$ ($x = 0, 0.03, 0.04, 0.06$) and their Mössbauer, crystal structure and magnetic properties

Minfeng Lü[1], Junjie Li[2], Xianfeng Hao[1], Zheng Yang[3], Defeng Zhou[1] and Jian Meng[1]

[1] Key Laboratory of Rare Earth Chemistry and Physics, Changchun Institute of Applied Chemistry, Chinese Academy of Sciences, Changchun 130022, People's Republic of China
[2] Jilin Province Petrochemical Engineering Institute, Changchun 130021, People's Republic of China
[3] Chang Chun Coal Design and Research Institute, Changchun 130021, People's Republic of China

E-mail: jmeng@ciac.jl.cn

Received 16 November 2007, in final form 10 March 2008
Published 7 April 2008
Online at stacks.iop.org/JPhysCM/20/175213

Abstract

Crystal structure and magnetization behavior of double perovskite compounds $Sr_2FeMo_{1-x}O_6$ ($x = 0, 0.03, 0.04, 0.06$) have been investigated using x-ray diffraction, Mössbauer spectroscopy and magnetization measurements. The proportion of Fe/Mo and the concentration of Mo vacancies determined by Rietveld methods and Mössbauer spectroscopy influence both the magnetic and magnetoresistive properties. An important fraction of the injected holes is localized at Mo sites, which is helpful for applications, because it promotes the occurrence of ordering between Fe and Mo cations. Both magnetic and Mössbauer spectroscopy data indicate that Mo hole doping strengthens the ferromagnetic interactions; moreover, ^{57}Fe Mössbauer spectroscopy revealed that the iron with one Mo vacancy existed inside regions of iron ions with one or two irons as first cation neighbors. A dramatic enhancement of the ferromagnetic order is due to the increased energy difference between the Fe and Mo sites.

(Some figures in this article are in colour only in the electronic version)

1. Introduction

Double perovskite $A_2BB'O_6$ (such as Sr_2FeMoO_6) compounds have attracted much attention due to their half-metallic nature and tunneling magnetoresistivity (TMR) at room temperature [1]. The origin of low-field magnetoresistivity has been attributed to the spin dependent scattering of electrons at grain boundaries [2]. The ideal structure of Sr_2FeMoO_6 can be viewed as a regular arrangement of corner-sharing FeO_6 and MoO_6 octahedra, alternating along all three directions of the crystal. The Sr cations reside in the cuboctahedral vacancies created by the corner-sharing octahedra. In a simple picture, the ferrimagnetic structure can be described as an ordered array of parallel Fe^{3+} ($S = 5/2$) magnetic moments coupled antiferromagnetically with Mo^{5+} ($S = 1/2$) spins. According to this model, the saturated magnetization (M_S) should be 4 μB in this compound. However, most experiments show reduced M_s [3–5], which could be attributed to the influence of antisite disorder at B and B′ sites. Due to the presence of antisite defects (ASDs), some Fe ions interact with their neighboring Fe ions and exhibit antiferromagnetism (AFM). Therefore, the M_s is decreased.

A completely new scheme of interactions has been proposed by Sarma *et al* [6]. Within this scenario, ferromagnetism (FM) and half metallicity are associated with the competition of hopping processes versus localization of electrons at the bare levels of the transition metal cations. The hopping of carriers leads to the appearance of a spin polarized

conduction band formed by the hybridization of Fe and Mo t_{2g} spin-down orbitals that couple antiferromagnetically with the magnetic moments of the localized electrons. In agreement with the experimental observations [7–10], the charge transfer due to the hopping mechanism produces an $Fe^{(3-\sigma)+}/Mo^{(5+\sigma)+}$ state with $0 < \delta < 1$. The roles of the structural effects in double perovskites are twofold: first, the stabilization of the band depends mostly on the B/B′ site energy difference [6] and the hopping interaction strengths between B and B′ cations [11, 12]; second, the structural defects are very likely to occur in this kind of complex transition metal oxides. Tovar *et al* [13] proposed that the Curie temperature of double perovskites is related to the density of states at the Fermi level ($D(E_F)$), and thus electron doping appeared as a natural strategy to modify their Curie temperature (T_c). Indeed, as reported in [14–18], partial substitution of trivalent La^{3+} or Nd^{3+} for divalent Sr^{2+} in Sr_2FeMoO_6 did influence its physical properties significantly; e.g., the T_c was increased, but the degree of cation ordering and magnetoresistance were reduced.

The Goldschmidt tolerance factor (t) is a semiquantitative estimate of how close an ABX_3 perovskite is to the cubic structure [19]. t is related to the radii r_i (i = A, B, X).

$$t = \frac{r_A + r_X}{\sqrt{2}(r_B + r_X)}. \quad (1)$$

A significant deviation of t from unity is not acceptable for stable perovskite structure. The tolerance factor can be adapted for double perovskites as well. In general, for double perovskites $A_2BB'_{(1-x)}O_6$ with mixed B/B′ site, the tolerance factor can be written as

$$t = \frac{r_A + r_O}{\sqrt{2}(\frac{r_B}{2} + \frac{r'_B(1-x)}{2} + r_O)} \quad (2)$$

where r_A, r_B, and $r_{B'}$ are the ionic radii of corresponding ions (for simplicity, we used ionic sizes of Fe^{3+} and Mo^{5+}, where $r_A = 1.44$ Å, $r_B = 0.645$ Å, $r_{B'} = 0.61$ Å and $r_O = 1.40$ Å). The calculated t for Sr_2FeMoO_6 is 0.990. Substitution at the B′ site with Mo vacancies (MoVs) brings the tolerance factor closer to unity, i.e. $x = 0.06$ gives $t = 0.9996$ and yields a more symmetrical lattice. However, the vacancies may be filled with Fe atoms, in which case ASDs were favored. Therefore, caution has to be taken in interpreting the observed changes of magnetic properties with MoV doping, steric effects or other side-effects, such as antisite disorder, off-stoichiometry, domain size and segregation of secondary phases.

In the light of this information, we prepared a series of $Sr_2FeMo_{1-x}O_6$ ($x = 0$, 0.03, 0.04, and 0.06) and investigated their magnetic behaviors and Mössbauer spectroscopy on the basis of structural characterization and analysis.

2. Experimental details

Samples of $Sr_2FeMo_{1-x}O_6$ ($x = 0$, 0.03, 0.04 and 0.06) were fabricated by the Pechini method [20]. Briefly, after dissolving analytical grade $Sr(NO_3)_2$, $Fe(NO_3)_3{\cdot}9H_2O$ and $(NH_4)_6Mo_7O_{24}{\cdot}4H_2O$ with the required molar ratio in citric acid (CA) solution, clear gels were obtained upon drying the sols at 150 °C for 5 h. Then the gels were ground in an agate mortar and then heated at 700 °C in air for 6 h. Finally, the precursors were pressed into pellets at 350 MPa and annealed at 1100 °C for 10 h in H_2/Ar (1%/99%) reducing flow. The temperature was elevated from room temperature to 1100 °C at a ramping speed of 5 °C min^{-1}. The samples were then slowly cooled at 5 °C min^{-1} down to room temperature under the reducing flow.

All products were characterized by x-ray powder diffraction (Rigaku, D/MAX-2500V) using Cu Kα radiation at 50 kV, 25 mA with a graphite monochromator. The refinement data were collected on the powder samples using a step scan mode with a step size of 0.02° and a counting time of 3 s per step in the 2θ range of 10°–120°. The unit cell of $Sr_2FeMo_{1-x}O_6$ was first determined from the x-ray powder diffraction patterns using indexing programs DICVOL04 [21] based on the first ten lines for the search of solutions. The XRD data were analyzed by the Rietveld method using the program GSAS [22] after excluding the impurity phases.

The size–microstrain analysis was carried out by x-ray line profile analysis (assuming a pseudo-Voigt function) using the XFIT software and the program BREADTH [23]. The analysis was complicated by the peak splitting arising from the distortion of the unit cell; therefore, constraints have been made by linking Lortz and FWHM terms. The instrumental broadening was corrected using a standard defect free Si sample.

Transport measurements were performed using a physical property measurement system (Quantum Design Co. Ltd) in the temperature range of 5–290 K. A standard four-probe technique was used. Magnetic measurements were carried out between 5 and 550 K with a commercial Quantum Design (SQUID) magnetometer or LakeShore VSM-735. Mössbauer spectra were investigated in the temperature range from 87 to 90 K using an Oxford MS-500 constant acceleration spectrometer. The velocity was calibrated with α-Fe foil.

3. Results and discussion

3.1. Results from x-ray Rietveld refinement

The enlarged XRD patterns of the synthesized samples at room temperature are shown in figure 1. The obtained samples were almost single phase except for a trace of impurities for the samples with high MoVs. For example, the striped phase and $SrMoO_4$ phase were found (less than 1%, respectively) for $x = 0.04$, and only the striped phase was detected in $x = 0.06$ (about 2%).The most relevant trend observed in the recorded patterns is the systematic increase of the diffraction intensity ratio $I(011)/[I(020) + I(112)]$. It varies from ∼0.02 for the undoped sample to ∼0.05 for $x = 0.04$ and ∼0.04 for the other MoVs doped samples. This implies that the samples with MoVs tend to improve the regular arrangement of B and B′ sites in the double perovskite structure. The diffraction patterns obtained can be successfully indexed and refined for all samples in the frame of the tetragonal space group $I4/m$, which is very common for slightly distorted double perovskites. Figure 2 shows the full

Table 1. Structural parameters for $Sr_2FeMo_{1-x}O_6$ at room temperature.

		x			
		0	0.03	0.04	0.06
	a (Å)	5.573 60(3)	5.572 31(2)	5.571 75(4)	5.571 50(3)
	c (Å)	7.900 10(8)	7.900 60(6)	7.898 76(9)	7.897 89(10)
	R_{wp} (%)	7.56	8.81	8.03	8.20
	R_p (%)	4.87	5.93	5.39	5.36
	R_F2 (%)	3.19	2.55	4.60	3.15
	χ^2	3.73	3.37	4.28	4.60
Sr	At (1/2 0 1/4)				
	Uiso (Å^2)	0.0106(3)	0.0111(1)	0.0117(5)	0.0106(3)
	occupancy	1	1	1	1
Fe1	At (0 0 0)				
	Uiso (Å^2)	0.0108(5)	0.0069(3)	0.0055(7)	0.0055(7)
	occupancy	0.795	0.904(6)	0.909(5)	0.880 (8)
Fe2	At (0 0 1/2)				
	Uiso (Å^2)	0.0108(5)	0.0069(3)	0.0055(7)	0.0055(7)
	occupancy	0.205	0.095(2)	0.090(5)	0.119(2)
Mo1	At (0 0 1/2)				
	Uiso (Å^2)	0.0059(3)	0.0069(3)	0.0055(7)	0.0055(7)
	occupancy	0.795	0.904(6)	0.894(8)	0.868 (9)
Mo2	At (0 0 0)				
	Uiso (Å^2)	0.0059(3)	0.0069(3)	0.0055(7)	0.0055(7)
	occupancy	0.205	0.065(2)	0.054(8)	0.071(1)
O1	At (0 0 z)	0.251(6)	0.252 (1)	0.252(6)	0.252(5)
	Uiso (Å^2)	0.0080(2)	0.0087(9)	0.0127(5)	0.0122(3)
	occupancy	1	1	1	1
O2	At (x y 0)				
	x	0.266 (7)	0.281 (6)	0.280(1)	0.277(2)
	y	0.236 (5)	0.224 (6)	0.228(1)	0.229(1)
	Uiso (Å^2)	0.0173(1)	0.0087(9)	0.0127(5)	0.0122(3)
	occupancy	1	1	1	1

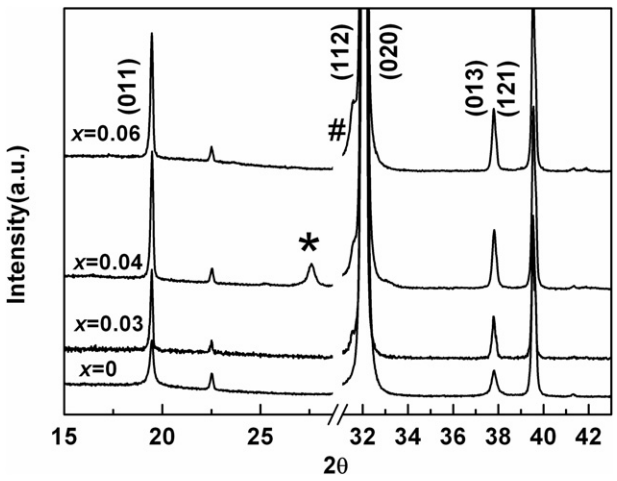

Figure 1. The enlarged x-ray pattern of the polycrystalline $Sr_2FeMo_{1-x}O_6$ series. The second phase ($SrMoO_4$ and striped phase) peaks are separately denoted by $*$ and #.

Rietveld profiles for the series refined at room temperature. In the refinement, the first one was a profile matching step, introduced by LeBail [24]. Here unit cell parameters, profile shape parameters and the individual Bragg intensities varied independently without referring to any structural model. In the second stage of Rietveld analysis, we refined the position and fractional occupancy of the atoms, holding the unit cell and profile shape parameters obtained in the first step. Constraint has been used in the third step, where the occupancies of Fe and Mo were varied while the total occupancy of Fe and Mo was kept equal to the stoichiometric ratio. Finally, the occupation of Mo was refined for all samples. The parameter for all samples did not change except for $x = 0.04$. The most important structural parameters and the discrepancy factors after the refinement are listed in table 1. The main interatomic lengths and angles are listed in table 2. One may argue that the refinement may be oversimplified, especially after neglecting the impurities. However, according to the above simple analysis, it is reasonable to believe that Fe/Mo ordering was favored unless the vacancies were filled with Fe atoms, in which case ASDs were favored. The changes of average ⟨Fe–O⟩ and ⟨Mo–O⟩ bond lengths with x are consistent with the principle that the apparent difference between the two bond lengths could account for a more complete Fe/Mo ordering. Otherwise equal Fe–O and Mo–O lengths could be derived as a result of complete disordering. Another significant issue should be mentioned: that our structural analysis is based on the Mössbauer results. It was found that the sample of $x = 0$,

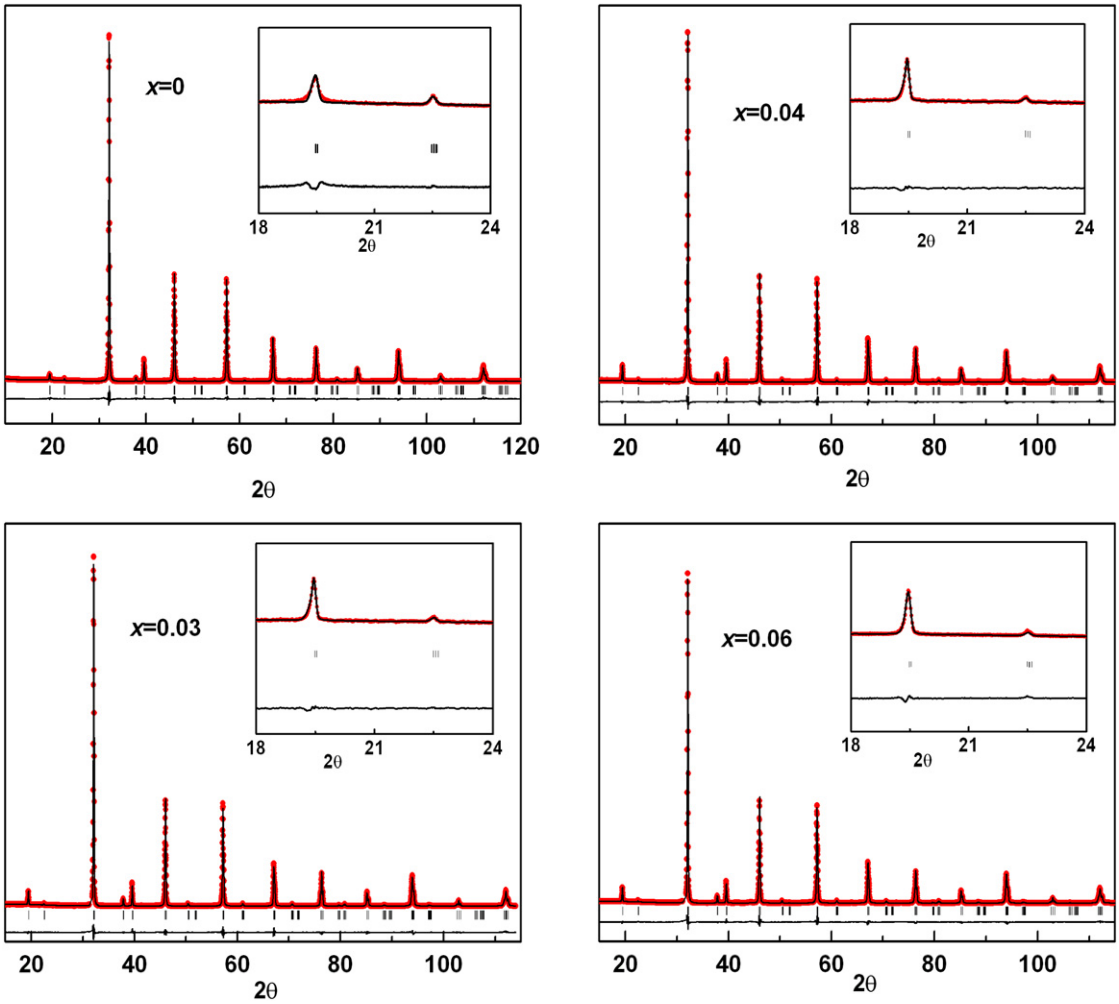

Figure 2. Observed (point) and calculated (continuous line) x-ray intensity profiles for the $Sr_2FeMo_{1-x}O_6$ series. The short vertical lines indicate the angular position of the allowed Bragg reflections. At the bottom in each figure the difference plot, $I_{obs} - I_{calc}$, is shown. The inset shows the low angle region.

Table 2. Selected bond lengths (Å) and angles (deg) for $Sr_2FeMo_{1-x}O_6$.

	x			
	0	0.03	0.04	0.06
Fe1–O1 × 2	1.988	1.992	1.995	1.994
Fe2–O2 × 4	1.986	2.007	2.012	2.003
Mo1–O1 × 2	1.962	1.958	1.954	1.954
Mo2–O2 × 4	1.961	1.958	1.948	1.954
⟨Fe–O⟩	1.987	2.002	2.006	2.000
⟨Mo–O⟩	1.961	1.958	1.950	1.954
Fe–O1–Mo	180.0(2)	180.0(2)	180.0(3)	180.0(6)
Fe–O2–Mo	173.0(4)	166.9(4)	168.1(2)	1690.0(1)

0.03 and 0.06 does contain $SrMoO_4$ phase, and three major iron environments can be distinguished (see below). Thus, we attribute the striped phase to part of the main phase. Therefore, the results of Rietveld show that the whole occupancy of Mo is about 0.95 in $x = 0.04$ (ignoring the actual occupancy of Sr), while the whole occupancy of Mo at the other samples is equal to the ratio from the experiment.

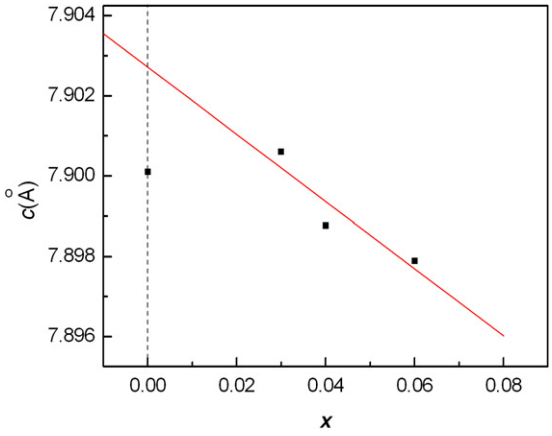

Figure 3. Changes in the c parameter in the $Sr_2FeMo_{1-x}O_6$ series.

In figure 3 we show the changes in the c parameter for the series. We find that the change of the c parameter with x in the MoV samples is roughly in agreement with Végard's law, because the extrapolated value when $x = 0$ is nearly 7.903 Å,

considerably larger than that of the $x = 0$ composition. This suggests that the effect of introducing new electrons is to increase the c parameter. In this case, it is necessary to recall that for electron doped compounds different local probes such as Mössbauer [25] and NMR [26] indicate that electrons tend to inject into the Mo sites. The charge difference between Fe and Mo became narrowed, and therefore the driving force for the B/B′ ordering reduced. Similar to the electron doping case, the increase of the B/B′ ordering due to the hole doping indicates that the charge difference between the cations on the Fe and Mo sites must be increased, since the spin-down subband shared between hybridized 3d(Fe) and 4d(Mo) orbitals crossing the Fermi level is likely to be partially filled with hole carriers.

3.2. Domain size analysis

In addition to structural information, domain size could also be quantitatively extracted from the high-resolution powder diffraction data. The domains are associated with the Fe/Mo ordering and size distribution. Our analysis is based on the double Voigt treatment of the peak broadenings exhibited by various classes of reflections. In this technique, the size and strain effects are approximated by a Voigt function [23], which is a convolution of Gaussian and Cauchy functions. The equivalent analytical expressions for the Warren–Averbach size–strain separation [27] were then obtained. The Fourier coefficient $F(L)$ in terms of distance, L, perpendicular to the diffracting planes is obtained by the Fourier transform of the Voigt function [23] and can be written as

$$F(L) = (-2L\beta_C - \pi L^2\beta_G^2) \tag{3}$$

where β_C and β_G are the Cauchy and Gauss components of the total integral breadth.

β_C and β_G can be written as

$$\beta_C = (\beta_{SC} + \beta_{DC}) \tag{4}$$

$$\beta_G^2 = (\beta_{SG}^2 + \beta_{DG}^2) \tag{5}$$

where β_{SC} and β_{DC} are the Cauchy components of the size and the strain integral breadth respectively and β_{SG} and β_{DG} are the corresponding Gaussian components.

Area and volume weighted domain sizes follow directly:

$$D_S = 1/2\beta_{SC} \tag{6}$$

$$\langle D\rangle_V = \frac{\exp(k^2)}{\beta_{SG}}\mathrm{erfc}(k) \tag{7}$$

where $k = \beta_{SC}/(\pi^{1/2}\beta_{SG})$ is the characteristic integral–breadth ratio of a Voigt function. Furthermore, the microstrain $\langle\varepsilon_L^2\rangle^{1/2}$ is given by

$$\langle\varepsilon_L^2\rangle^{1/2} = [\beta_{DG}^2/(2\pi) + \beta_{DC}/(\pi^2 L)]/S^2 \tag{8}$$

where $S = \frac{2\sin\theta}{\lambda}$

The volume weighted column-length distribution function is given by

$$P_v(L) \propto L\frac{\mathrm{d}^2 A_S(L)}{\mathrm{d}L^2}. \tag{9}$$

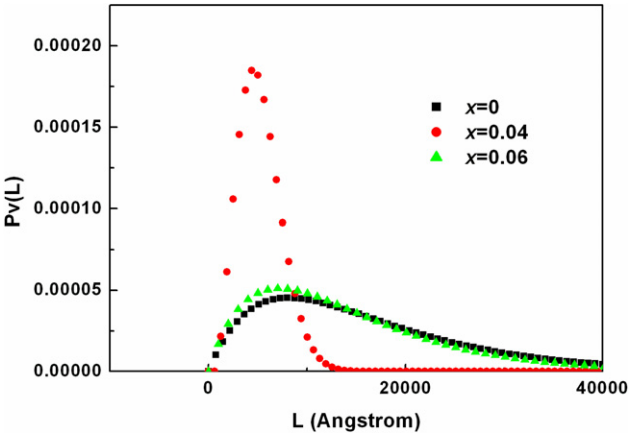

Figure 4. Volume weighted column-length distribution function for the $Sr_2FeMo_{1-x}O_6$ samples.

For a size-broadened profile, the size coefficient is

$$A_S(L) = \exp(-2L\beta_{SC} - \pi L^2\beta_{SG}^2). \tag{10}$$

To obtain this information, a proper analysis of the splitting peak broadenings of each pattern, and a whole-pattern fitting approach, is necessary. However, the analysis was complicated by the peak splitting arising from the distortion of the perfect perovskites. We postulated that each peak has the same Lorentzian and FWHM. The FWHM and 2θ positions of the 011, 013 reflections were then determined. For comparative purposes, similar analysis has been carried out for 020, 022, 004, 220 and 024 reflections. The Cauchy and Gaussian components of the size and strain broadened profiles were then separated. The results of the double Voigt method for the series are listed in table 3 The ordered domain size is smaller than the volume weighted crystallite size due to the presence of antiphase boundaries in the Fe/Mo ordering [28] for the whole series. A second feature for the Warren–Averbach size–strain analysis is that the ordered domain size of $x = 0$ is smaller than those of $x = 0.04$ and 0.06, which is also in agreement with the magnetization and Mössbauer results. The degree of electronic transportation at the same time is expected to depend on the size of the ordered domains, because cation disorder leads to electrically insulating domains in the otherwise half-metallic double perovskites. Most significantly, the volume weighted crystallite size of $x = 0.04$ is smaller than its counterpart. The volume weighted column-length distribution function $P_v(L)$ obtained from 020, 022, 004, 200 and 024 reflections has been shown in figure 4, from which we can see that the column-length distribution is much narrower for the sample of $x = 0.04$; the smaller particles may display super-paramagnetic behaviors. Considering the approximations employed, the true value may be somewhat deviated. However there is no doubt that the paramagnetic behavior which was observed in Mössbauer measurement of $x = 0.04$ at 90 K is related to the coherent length of crystallite size.

3.3. Magnetic properties

A saturation magnetization is first evaluated for the simplest ferrimagnetic arrangements (model FIM) [5], which leads to

Table 3. Results of double Voigt method for the series.

Sample		D_s (Å)	$\langle\varepsilon_L^2\rangle^{1/2}_{L=\langle D\rangle_S/2}$ (10^{-3})	$\langle D\rangle_V$ (Å)	$\langle\varepsilon_L^2\rangle^{1/2}_{L=\langle D\rangle_V/2}$ (10^{-3})
x =0	Odd–odd–odd reflections	470 ± 20	0.82 ± 0.06	670 ± 20	0.71 ± 0.05
	Even–even–even reflections	8100 ± 1600	0.35 ± 0.01	16 300 ± 3300	0.32 ± 0.01
x = 0.04	Odd–odd–odd reflections	1700 ± 160	0.14 ± 0.03	2 200 ± 150	0.13 ± 0.03
	Even–even–even reflections	4500 ± 650	0.22 ± 0.01	5 300 ± 400	0.21 ± 0.01
x = 0.06	Odd–odd–odd reflections	1900 ± 200	0.26 ± 0.03	2 500 ± 200	0.24 ± 0.02
	Even–even–even reflections	7200 ± 1900	0.26 ± 0.01	14 400 ± 3900	0.23 ± 0.01

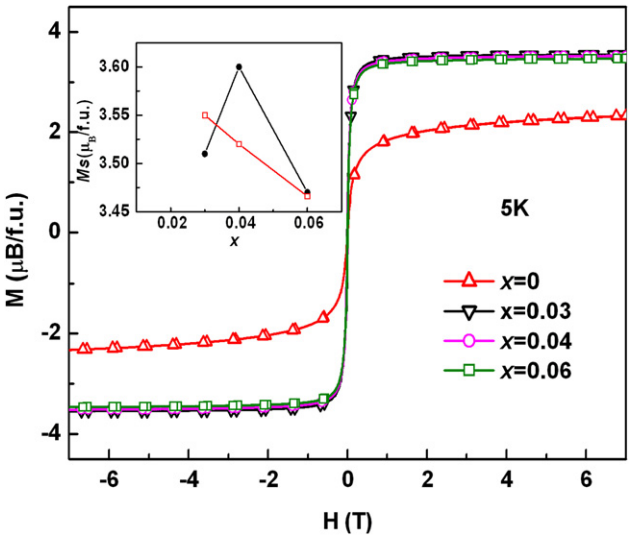

Figure 5. Field dependence of magnetization of the $Sr_2FeMo_{1-x}O_6$ samples taken at 5 K. Inset: dependence of saturation magnetization on doping content x. The open square is the experimental value; the filled circle represents the calculated value based on the FIM and the vacancy contribution.

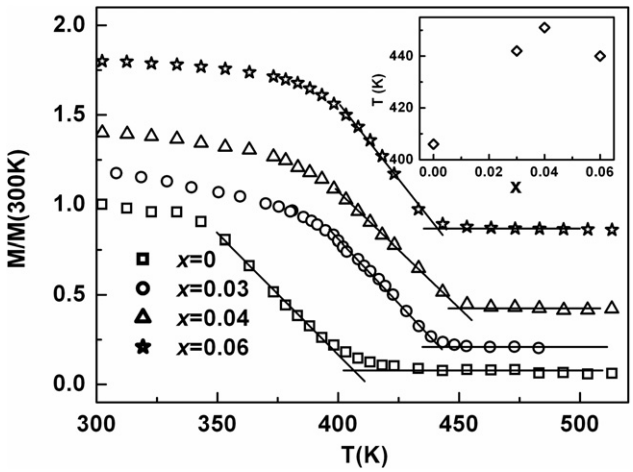

Figure 6. Temperature dependence of low-field (500 Oe) dc normalized magnetization for the $Sr_2FeMo_{1-x}O_6$ samples. Inset: the evolution of the T_c for the series.

$M_s = (4 - 8p)$, where p is the concentration of antisite defects. The calculated result gives 2.36 μB/f.u. for the sample without doping ($x = 0$), which is close to the experimental result of 2.32 μB/f.u. M_s of the MoV doping samples was then evaluated by the formula $M_s = 5(1 - 2r) - (t - 2v)$ μ_B, where model FIM [5] was again used, which assumes that an antiferromagnetic coupling between B and B′ produces a net magnetization. r is the concentration of Fe ions filled at B′ sublattices, v is the concentration of Mo ions filled at B sublattices, and t means the Mo concentration of the experiment. The calculated saturation magnetization is 3.21 μB/f.u. for $x = 0.03$, 3.24 μB/f.u. for $x = 0.04$, and 3.01 μB/f.u. for $x = 0.06$ respectively. The deviations from experimental results (see figure 5) could be due to the improvement of net saturation magnetization by removing some down spin localized moments and hole doping effects. The estimated increases of magnetization are 0.12 μB/f.u. for 1% MoV sample of $x = 0.03$, 0.07 μB/f.u. for $x = 0.04$, and 0.076 μB/f.u. for $x = 0.06$. Compared with the value given by Retuerto *et al* [29] for 0.06 doping (the estimated increase of magnetization is 0.11 μB/f.u. for 1% MoVs), the decrease of magnetization for $x = 0.04$ and 0.06 could be explained by the presence of impurity phases. In order to estimate the hole doping effect, we use $Sr_2Fe^{3+}Fe_o^{3+}Mo^{5+}O_6$, where Fe_o^{3+} means that the MoVs are located at the B sites, which has a similar effect to Fe^{3+}. M_S leads to $5(1 - 2r + 2w) - (t - 2v)$, where w is the concentration of MoVs at the B sublattices. In this case, the concentration of MoVs is equal to the fraction of unoccupied atoms. The difference between the experimental M_s and the calculated one using the final equation for every MoV sample is shown in the inset of figure 5. The final calculated results are in agreement with the observed ones. Figure 6 shows the temperature evolutions of magnetization for compounds with all doping concentrations around T_c. All curves were normalized at 300 K and shifted up for the sake of clarity. The transition temperature T_c is given by extrapolating the magnetization in the transition region to zero magnetization. The values of T_c of the MoV samples are much higher than that of the undoped sample. This suggests that the ordered Fe/Mo structure strengthens the ferromagnetic exchange, and enhances T_c. Recent work using a three-band model Hamiltonian [30] led to an increase in T_c with the degree of the Fe/Mo ordering only up with 0.9; beyond this the further increase in the Fe/Mo ordering decreased with T_c. Alonso *et al* also suggested that the ferromagnetic order of next-nearest-neighbor Fe ions in Mo–Fe–Fe–Fe–Mo arrangements should be favored due to strongly antiferromagnetic (AFM) superexchange interactions between the nearest-neighbor Fe ions at regular and irregular (antisite) positions [31]. The normalized Fe/Mo ordering $g/(1 + f)$, where g and f are the occupation of Fe and MoVs at the B sites, for $x = 0.03$, 0.04, and 0.06, is 0.88, 0.88, and 0.86,

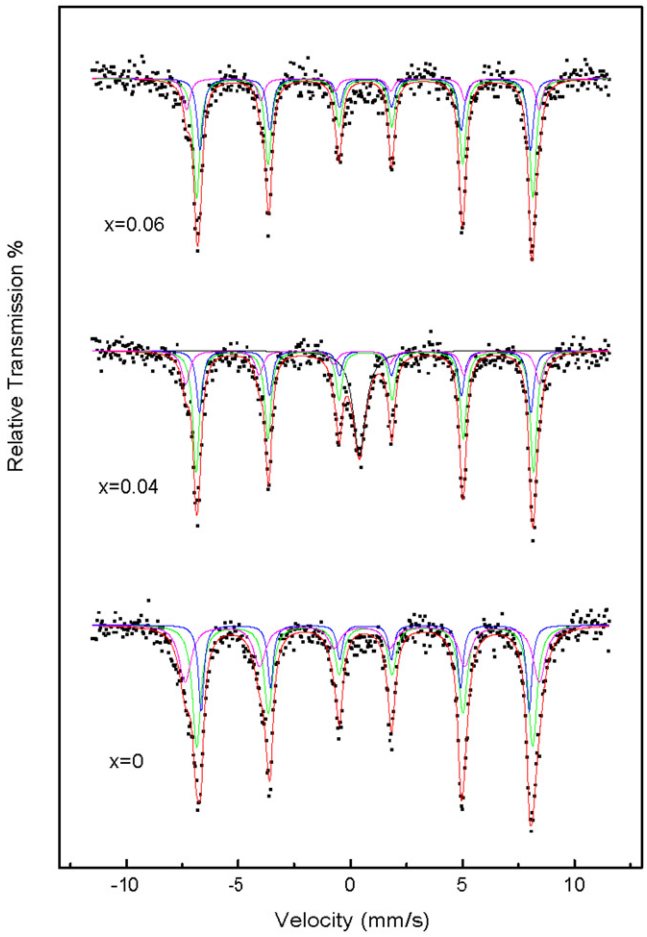

Figure 7. Low-temperature Mössbauer spectra recorded for the $Sr_2FeMo_{1-x}O_6$ samples. The solid lines are best fits to the experimental data discussed in the text.

smaller than 0.9. Therefore, the evolution of T_c is consistent with the above rule. Therefore, ferromagnetic exchange is favored when MoVs are located at the B sites; their effect is similar to Fe^{3+}. The existence of MoVs instead of non-magnetic Mo ions also prevents a dilution effect (–Mo–Fe–Mo–Mo–Mo–Fe–) of the ferromagnetic interactions among Fe ions, which counterbalance the enhancement due to AFM nearest-neighbor interactions. Similar experimental evidence was also confirmed by Rubi *et al* [32].

3.4. Mössbauer spectrometry

In order to monitor the suggested change of ferromagnetic coupling, Mössbauer spectra were collected at several temperatures between 87 and 90 K and representative data are shown in figure 7. As mentioned before, antisite defects can occur in the structure where an Fe ion takes the place of a Mo ion on the B′ site or vice versa. Consequently not all iron ions experience the same first cation neighbor environment. Iron in the perfect NaCl-type superstructure has a total of six molybdenum first cation neighbors at the B′ sites. However, the misplaced iron ions at the B′ sites have a total of six iron ions at the neighboring B sites, while these last six iron ions experience an environment of five molybdenum and one iron ion at their neighboring B′ sites. As the antisite defects are greater than 6%, the probability of finding iron ions with more iron as first cation neighbor is relatively high [33]. Therefore, the concentration of antisite defects p should involve the iron cations with two, three, four and five irons as first cation neighbors.

Table 4. Mössbauer fitting parameters for the series, δ, Q_s, H_{hf} and Γ, accounting for the isomer shift, the quadrupole splitting, the hyperfine field and the half-height width, respectively. The antisite concentration (p) is mainly deduced from the absorption areas of the third components. Typical errors are ± 0.01 mm s^{-1} for δ, Q_s and $\Gamma/2$, ± 0.5 T for H_{hf}, $\pm 3\%$ for area and $\pm 0.5\%$ for p.

x (K)	δ (mm s^{-1})	Q_s (mm s^{-1})	H_{hf} (T)	$\Gamma/2$ (mm s^{-1})	Area ratio (%)	p (%)
0, 90	0.72	0.02	45.3	0.15	22	
	0.70	0.04	46.4	0.22	47	
	0.57	0	48.9	0.32	31	22
0.04, 90	0.72	0.01	45.8	0.16	22	
	0.71	0.04	46.6	0.17	45	
	0.57	−0.05	48.9	0.21	15	13
	0.45	0.03	—	0.33	18	
0.06, 87	0.72	0	45.7	0.16	30	
	0.70	0.03	46.5	0.17	53	
	0.60	0	48.8	0.18	17	14

We distinguish three major iron environments for $x = 0$. The first component with the smallest absorption area corresponds to iron cations in a perfectly ordered environment with six Mo first cation neighbors; its Mössbauer parameters agree well with those reported in [7] for Sr_2FeMoO_6. The corresponding value of isomer shift is always slightly higher, and the hyperfine magnetic field is lower than that of the other two components. This reflects a considerable electron density on the minority spin t_{2g} level of iron, which is in agreement with the existence of a high degree of hybridization between 3d(Fe) and 4d(Mo) energy levels. The second magnetic component in the ^{57}Fe Mössbauer spectrum was also detected earlier [33]. This component, with the largest absorption area, intermediate value of isomer shift and hyperfine magnetic field, originates from iron cations having one or two iron ions as their first cation neighbor environment. This refers to a decreased electron density at the minority spin level of iron [34]. The decreased minority spin electron density can be interpreted as a reduced degree of delocalization of the $4d^1$ electron of Mo. The third component with the lowest isomer shift and the greatest hyperfine field corresponds to the iron cations having six, five, four and three irons as first cation neighbors. The relatively larger absorption area expected to be present in $x = 0$ is thought to be responsible for the presence of high extent of antisite defects, which is in agreement with the analysis of ordered domain size and the results of structure and magnetism of $x = 0$. The fitted parameters are listed in table 4.

In $x = 0.04$, the central paramagnetic signal is as noticeable as that of [35], comprising 18% of the total area. Jacobe *et al* referred it to a result of the wet preparation method that produced particles with a size distribution, with the smaller ones displaying a super-paramagnetic regime [36]. In our case, the $SrMoO_4$ phase has been identified in the x-ray diffraction

pattern, and another important issue that should be addressed is that the volume weighted column-length distribution obtained from 020, 022, 004, 200 and 024 reflections has shown the possibility of the presence of the smaller particles. The phase should most likely be the paramagnetic impurity phase with a small amount of $SrMoO_4$, but it is impossible to exclude the presence of super-paramagnetic component. The isomer shift is ∼0.45 mm s^{-1}, indicating that it probably originates from iron cations with the least degree of hybridization. In reality the actual composition of this phase includes a considerable amount of iron. The magnetic sextet was fitted using three principal components with hyperfine fields ranging from 46 to 49 T. The hyperfine data are compared with those given for $x = 0$ in table 4.

In contrast with ^{57}Fe Mössbauer studies for the $x = 0$ sample with high levels of cation disorder, it is strongly reminiscent of the $x = 0.06$ sample with MoVs. However, the 87 K data were also fitted using a combination of three different hyperfine components as shown in table 4. The component with the smallest absorption area, which has been mentioned early, corresponds to iron ions that have three or more iron first cation neighbors, as Mössbauer spectroscopy can give important information about the nature of the defects. One could observe magnetic Zeeman sextets with well resolved Lorentzian lines, but the remaining two main magnetic components are needed to describe each sextuplet spectrum. On one hand, the isomer shift values and hyperfine magnetic field of the component in $x = 0.06$ remain close to 0.72 mm s^{-1} and 45.7 T respectively. As typically observed in our samples, this is unambiguously characteristic of iron cations in a perfectly ordered environment with six Mo first cation neighbors. On the other hand, the secondary magnetic components with the largest absorption area show close values of δ and H_{hf} to those of $x = 0$, originating from iron cations that have one or two iron ions in their first cation neighbor environment. This component is also thought to be due to the presence of MoVs near the Fe site. Reduced electron density in the vicinity of MoVs would cause an enhancement of the magnetic hyperfine field, and also decrease the shift.

From the relative magnitudes of the absorption areas of different components we can evaluate the concentration of antisite defects p using the equation

$$q_n = [6!/(n!(6-n)!)][(1-p)^{(n+1)}p^{(6-n)} + (1-p)^{(6-n)}p^{(n+1)}] \quad (11)$$

where q_n is the probability of finding an iron ion with n number of molybdenum ions as first cation neighbors. By comparing the q_n values and the absorption areas of the three components of $x = 0$, and the third component of $x = 0.04$ and 0.06, we evaluate the concentration of antisite defects for the all samples. This agrees quite well with the value obtained by the x-ray analysis (table 4). However, the absorption area of the second component of $x = 0.06$ should be about 48%, and the discrepancy originates from the presence of one MoV in their first cation neighbor environment. We can evaluate the concentration of MoVs, which is approximately equal to one-sixth of the residual area of the secondary component. By using the equation, we can evaluate the concentration of MoVs which is about 5% in the $x = 0.06$ sample, which is in agreement with the refinement analysis. This is strongly reminiscent of the scenario that strong antiferromagnetic superexchange coupling between Fe occupying regular sites and their near-neighbor iron not only stabilizes the half-metallic ferromagnetic states but also strengthens ferromagnetic interaction between the next-nearest-neighbor Fe [30]. This finding also suggests that the role of the Fe ions with one MoV as their neighbor is similar to that of iron ions with one iron as first cation neighbor. The iron sites with one MoV lie higher in energy in the absence of spin-down electrons than those with none, and the spin-down electrons spend less time on these sites, leading to the lower isomer shifts. Since MoVs are not involved in hopping interaction, a dramatic enhancement of the ferromagnetic order is due to the increased energy difference between the B and B′ sites. Another significant issue that should be addressed is to clarify that the absorption area of the first component in the $x = 0.04$ sample is 22%, while the calculated value should be about 37%. The distinction is in accordance with the presence of a considerable amount of iron in the paramagnetic phase of the $x = 0.04$ sample.

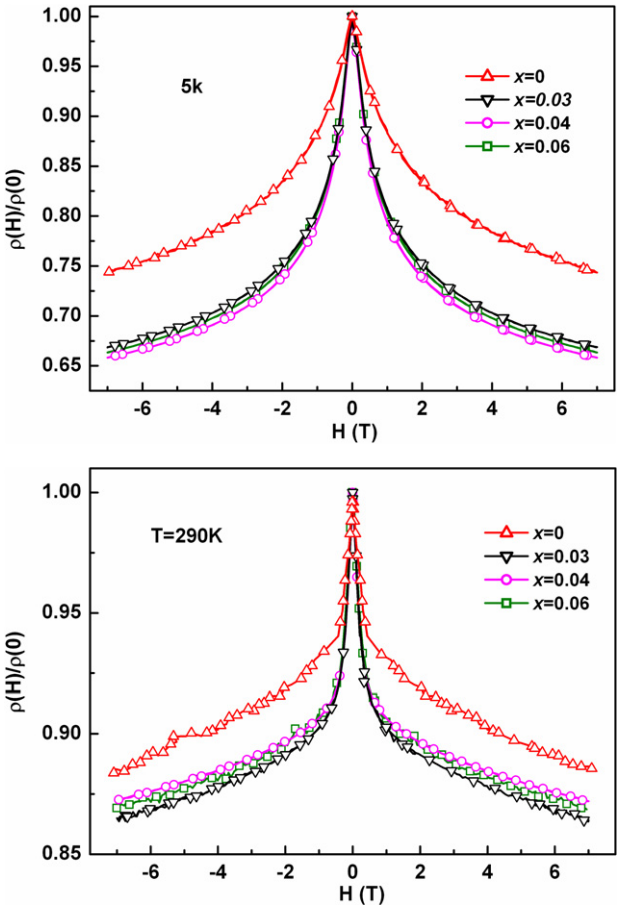

Figure 8. $\rho(H)/\rho(0)$ versus applied external field for the $Sr_2FeMo_{1-x}O_6$ samples at (a) 5 and (b) 290 K.

3.5. Magnetotransport measurements

Figure 8 presents $\rho(H)/\rho(0)$ recorded at various temperatures as a function of applied field with PPMS. The magnetoresistance, MR, is defined as MR $= (\rho(0) - \rho(H))/\rho(0)$. It is

seen that the $\rho(H)/\rho(0)$ ratio exhibits a distinct enhancement at 5 and 300 K, by comparing the MoV samples with the pristine one. For example, at 5 K, $x = 0.04$ reaches the maximum value (>34%) for $H = 7$ T. However, moderate improvement (<26%) could be achieved for $x = 0$. Therefore, the MR properties at low temperature should connect with the normalized Fe/Mo order, especially for $x = 0.04$, which is consistent with the T_c. At 290 K other comparable figures are obtained: the MR ratio at 0.3 T is 6.6% and at 1 T it reaches 9.8% for $x = 0.03$, while the MR value at 0.3 T for $x = 0$ reaches 4.9%. There is an important low-field component of MR, implying a fast saturation of MR under low magnetic field and room temperature. The relatively high extent of cation order and small number of MoVs expected to be present in our MoV samples is thought to be responsible for the improved magnetoresistive properties at room temperature. Since the MoV sample sharply differs from $x = 0$ in the extent of Fe/Mo ordering, the low-field rapid variation in MR evidently arises from the long-range order, leading to a half-metallic ferromagnetic state and consequent strong intergrain spin-dependent scattering, although MoV doping would decrease the concentration of spin-polarized electrons.

4. Conclusion

We have synthesized the solid solution $Sr_2FeMo_{1-x}O_6$ over a small range of compositions. Detailed x-ray diffraction results establish that the Mo valency at the B sites over the entire range of x maintained the character of a formal trivalent Fe^{3+} state, combined with an analysis of the magnetic moment. Additionally, ^{57}Fe Mössbauer spectroscopy further certified that iron with one Mo vacancy existed inside regions of iron ions with one or two irons as first cation neighbors. An important fraction of the injected holes is localized at Mo sites, which is helpful for applications, because it promotes the occurrence of ordering between Fe and Mo cations.

Acknowledgments

We are grateful for financial support from the National Natural Science Foundation of China (20771100, 20671088, 20601026, 20331030).

References

[1] Kobayashi K-I, Kimura T, Sawada H, Terakura K and Tokura Y 1998 *Nature* **395** 667
[2] Kim T H, Uehara M, Cheong S-W and Lee S 1999 *Appl. Phys. Lett.* **74** 1737
[3] Niebieskikwiat D, Sánchez R D, Caneiro A, Morales L, Vásquez-Mansilla M, Rivadulla F and Hueso L E 2000 *Phys. Rev.* B **62** 3340
[4] Tomioka Y, Okuda T, Okimoto Y, Kumai R, Kobayashi K-I and Tokura Y 2000 *Phys. Rev.* B **61** 422
[5] Balcells Ll, Navarro J, Bibes M, Roig A, Martínez B and Fontcuberta J 2001 *Appl. Phys. Lett.* **78** 781
[6] Sarma D D, Mahadevan P, Saha-Dasgupta T, Ray S and Kumar A 2000 *Phys. Rev. Lett.* **85** 2549
[7] Lindén J, Yamamoto T, Karppinen M, Yamauchi Y and Pietari T 2000 *Appl. Phys. Lett.* **76** 2925
[8] Greneche J M, Venkatesan M, Suryanarayanan R and Coey J M D 2001 *Phys. Rev.* B **63** 174403
[9] Karppinen M, Yamauchi H, Yasukawa Y, Linden J, Chan T S, Liu R S and Chen J M 2003 *Chem. Mater.* **15** 4118
[10] Kapusta Cz, Riedi P C, Zajac D, Sikora M, De Teresa J M, Morellon L and Ibarra M R 2002 *J. Magn. Magn. Mater.* **242–245** 701
[11] Ritter C, Ibarra M R, Morellon L, Blasco J, Garća J and De Teresa J M 2000 *J. Phys.: Condens. Matter* **12** 8295
[12] Frontera C, Rubi D, Navarro J, Garća-Muñoz J L and Fontcuberta J 2003 *Phys. Rev.* B **68** 012412
[13] Tovar M, Causa M T, Butera A, Navarro J, Martínez B, Fontcuberta J and Passeggi M C G 2002 *Phys. Rev.* B **66** 024409
[14] Navarro J, Frontera C, Balcells L, Martínez B and Fontcuberta J 2001 *Phys. Rev.* B **64** 092411
[15] Serrate D, De Teresa J M, Blasco J, Ibarra M R, Morellón L and Ritter C 2002 *Appl. Phys. Lett.* **80** 4573
[16] Serrate D, De Teresa J M, Blasco J, Ibarra M R, Morellón L and Ritter C 2004 *Eur. Phys. J.* B **39** 35
[17] Navarro J, Nogués J, Muñoz J S and Fontcuberta J 2003 *Phys. Rev.* B **67** 174416
[18] Rubi D, Frontera C, Herranz G, García Muñoz J L, Fontcuberta J and Ritter C 2004 *J. Appl. Phys.* **95** 7082
[19] Goldschmidt V M 1927 *Ber. Dtsch. Chem. Ges.* **60** 1263
[20] Lü M F, Wang J P, Liu J F, Hao X F, Zhou D F, Wu Z J and Meng J 2006 *Appl. Phys. Lett.* **89** 092505
[21] Boultif A and Louer D 2004 *J. Appl. Crystallogr.* **37** 724
Louer D and Louer M 1972 *J. Appl. Crystallogr.* **5** 271
Boultif A and Louer D 1991 *J. Appl. Crystallogr.* **24** 987
[22] Larson A C and von Dreele R B 1994 *GSAS: General Structure Analysis System ANSCE, MS-H805* (Los Alamos, NM: Los Alamos National Laboratory)
[23] Balzar D and Ledbetter H 1993 *J. Appl. Crystallogr.* **26** 97
[24] LeBail A, Duroy H and Fourquet J L 1988 *Mater. Res. Bull.* **23** 447
[25] Yasukawa Y, Lindén J, Chan T S, Liu R S, Yamauchi H and Karppinen M 2004 *J. Solid State Chem.* **177** 2655
[26] Wojcik M, Jedryka E, Nadolski S, Navarro J, Rubi D and Fontcuberta J 2004 *Phys. Rev.* B **69** 100407
[27] Warren B E and Averbach B L 1950 *J. Appl. Phys.* **21** 595
[28] Woodward P M, Hoffmann R D and Sleight A W 1994 *J. Mater. Res.* **9** 2118
[29] Retuerto M, Alonso J A, Martínez-Lope M J, Martínez J L and García-Hernández M 2004 *Appl. Phys. Lett.* **85** 266
[30] Solovyev I V 2002 *Phys. Rev.* B **65** 144446
[31] Alonso J L, Fernández L A, Guinea F, Lesmes F and Martín-Mayor V 2003 *Phys. Rev.* B **67** 214423
[32] Rubi D, Frontera C, Roig A, Nogués J, Muñoz J S and Fontcuberta J 2005 *J. Phys.: Condens. Matter* **17** 8037
[33] Douvalis A P, Venkatesan M, Velasco P, Fitzgerald C B and Coey J M D 2003 *J. Appl. Phys.* **93** 8071
[34] Klencsár Z, Németha Z, Vértesa A, Kotsis I, Nagy M, Cziráki Á, Ulhaq-Bouillet C, Pierron-Bohnes V, Vad K, Mészáros S and Hakl J 2004 *J. Magn. Magn. Mater.* **281** 115
[35] Algarabel P A, Morellon L, De Teresa J M, Blasco J, Garćia J, Ibarra M R, Hernández T, Plazaola F and Barandiarán J M 2001 *J. Magn. Magn. Mater.* **226–230** 1089
[36] Jacoboa S E, Duhaldea S and Mercader R C 2004 *Physica* B **354** 59